View metadata, citation and similar papers at core.ac.uk

brought to you by CORE

provided by HKU Scholars Hub

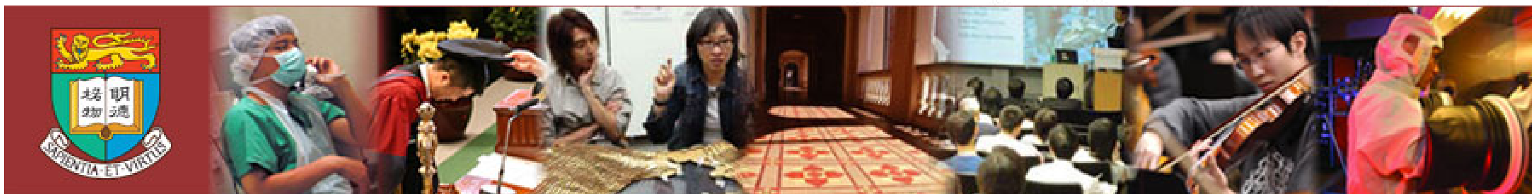

Title	Robust source and mask optimization compensating for mask topography effects in computational lithography
Author(s)	Li, J; Lam, EYM
Citation	Optics Express, 2014, v. 22 n. 8, p. 9471-9485
Issued Date	2014
URL	http://hdl.handle.net/10722/200619
Rights	Optics Express. Copyright © Optical Society of America.

Robust source and mask optimization compensating for mask topography effects in computational lithography

Jia Li and Edmund Y. Lam[*]
Imaging Systems Laboratory, Department of Electrical and Electronic Engineering, The University of Hong Kong, Pokfulam, Hong Kong, China
[*]elam@eee.hku.hk

Abstract: Mask topography effects need to be taken into consideration for a more accurate solution of source mask optimization (SMO) in advanced optical lithography. However, rigorous 3D mask models generally involve intensive computation and conventional SMO fails to manipulate the mask-induced undesired phase errors that degrade the usable depth of focus (uDOF) and process yield. In this work, an optimization approach incorporating pupil wavefront aberrations into SMO procedure is developed as an alternative to maximize the uDOF. We first design the pupil wavefront function by adding primary and secondary spherical aberrations through the coefficients of the Zernike polynomials, and then apply the conjugate gradient method to achieve an optimal source-mask pair under the condition of aberrated pupil. We also use a statistical model to determine the Zernike coefficients for the phase control and adjustment. Rigorous simulations of thick masks show that this approach provides compensation for mask topography effects by improving the pattern fidelity and increasing uDOF.

© 2014 Optical Society of America

OCIS codes: (110.4235) Nanolithography; (110.5220) Photolithography; (110.1758) Computational imaging.

References and links

1. J. Choi, I.-Y. Kang, J. S. Park, I. K. Shin, and C.-U. Jeon, "Manufacurability of computation lithography mask: Current limit and requirements for sub-20nm node," in *Optical Microlithography XXVI*, W. Conley, ed. (2013), vol. 8683 of *Proc. SPIE*, p. 86830L.
2. V. Agudelo, P. Evanschitzky, A. Erdmann, T. Fühner, F. Shao, S. Limmer, and D. Fey, "Accuracy and performance of 3D mask models in optical projection lithography," in *Optical Microlithography XXIV*, M. V. Dusa, ed. (2011), vol. 7973 of *Proc. SPIE*, p. 79730O.
3. J. Finders and T. Hollink, "Mask 3D effects: Impact on imaging and placement," in *27th European Mask and Lithography Conference*, U. F. Behringer, ed. (2011), vol. 7985 of *Proc. SPIE*, p. 79850I.
4. A. Erdmann, F. Shao, P. Evanschitzky, and T. Fühner, "Mask-topography-induced phase effects and wave aberrations in optical and extreme ultraviolet lithography," J. Vac. Sci. Technol. B **28**, C6J1–C6J7 (2010).
5. G.-S. Yoon, H.-B. Kim, J.-W. Lee, S.-W. Choi, and W.-S. Han, "Phase-shifted assist feature OPC for sub-45 nm node optical lithography," in *Optical Microlithography XX*, D. G. Flagello, ed. (2007), vol. 6520 of *Proc. SPIE*, p. 65201A.
6. T. Fühner, P. Evanschitzky, and A. Erdmann, "Mutual source, mask and projector pupil optimization," in *Optical Microlithography XXV*, W. Conley, ed. (2012), vol. 8326 of *Proc. SPIE*, p. 83260I.
7. M. K. Sears and B. Smith, "Modeling the effects of pupil-manipulated spherical aberration in optical nanolithography," J. Micro/Nanolith., MEMS, MOEMS **12**, 013008 (2013).
8. A. K. Wong and A. R. Neureuther, "Mask topography effects in projection printing of phase phifting masks," IEEE Trans. on Electron Devices **41**, 895–902 (1994).

#205715 - $15.00 USD Received 29 Jan 2014; revised 4 Apr 2014; accepted 4 Apr 2014; published 11 Apr 2014

9. M. G. Moharam, E. B. Gram, and D. A. Pommet, “Formulation for stable and efficient implementation of the rigorous coupled-wave analysis of binary gratings,” J. Opt. Soc. Am. A **12**, 1068–1076 (1995).
10. F. Shao, P. Evanschitzky, D. Reibold, and A. Erdmann, “Fast rigorous simulation of mask diffraction using the waveguide method with parallelized decomposition technique,” in *24th European Mask and Lithography Conference*, U. F. W. Behringer, ed. (2008), vol. 6792 of *Proc. SPIE*, p. 679206.
11. T. H. Coskun, H. Dai, H.-T. Huang, V. Kamat, and C. Ngai, “Accounting for mask topography effects in source-mask optimization for advanced nodes,” in *Optical Microlithography XXIV*, M. V. Dusa, ed. (2011), vol. 7973 of *Proc. SPIE*, p. 79730P.
12. E. Y. Lam and A. K. Wong, “Computation lithography: Virtual reality and virtual virtuality,” Opt. Express **17**, 12259–12268 (2009).
13. E. Y. Lam and A. K. Wong, “Nebulous hotspot and algorithm variability in computation lithography,” J. Micro/Nanolith. MEMS MOEMS **9**, 033002 (2010).
14. M. Fakhry, Y. Granik, K. Adam, and K. Lai, “Total source mask optimization: High-capacity, resist modeling, and production-ready mask solution,” in *Photomask Technology 2011*, W. Maurer and F. E. Abboud, eds. (2011), vol. 8166 of *Proc. SPIE*, p. 81663M.
15. J. Li, S. Liu, and E. Y. Lam, “Efficient source and mask optimization with augmented Lagrangian methods in optical lithography,” Opt. Express **21**, 8076–8090 (2013).
16. X. Ma, C. Han, Y. Li, L. Dong, and G. R. Arce, “Pixelated source and mask optimization for immersion lithography,” J. Opt. Soc. Am. A **30**, 112–123 (2013).
17. T. Dam, V. Tolani, P. Hu, K.-H. Baik, L. Pang, B. Gleason, S. D. Slonaker, and J. K. Tyminski, “Source-mask optimization (SMO): from theory to practice,” in *Optical Microlithography XXIII*, M. V. Dusa and W. Conley, eds. (2010), vol. 7640 of *Proc. SPIE*, p. 764028.
18. M. K. Sears, G. Fenger, J. Mailfert, and B. Smith, “Extending SMO into the lens pupil domain,” in *Optical Microlithography XXIV*, M. V. Dusa, ed. (2011), vol. 7973 of *Proc. SPIE*, p. 79731B.
19. H. Aoyama, Y. Mizuno, N. Hirayanagi, N. Kita, R. Matsui, H. Izumi, K. Tajima, J. Siebert, W. Demmerle, and T. Matsuyama, “Impact of realistic source shape and flexibility on source mask optimization,” J. Micro/Nanolith. MEMS MOEMS **13**, 011005 (2014).
20. V. Agudelo, P. Evanschitzky, A. Erdmann, and T. Fühner, “Evaluation of various compact mask and imaging models for the efficient simulation of mask topography effects in immersion lithography,” in *Optical Microlithography XXV*, W. Conley, ed. (2012), vol. 8326 of *Proc. SPIE*, p. 832609.
21. A. K. Wong, *Optical Imaging in Projection Microlithography* (SPIE, 2005, Chap. 2).
22. N. Jia and E. Y. Lam, “Pixelated source mask optimization for process robustness in optical lithography,” Opt. Express **19**, 19384–19398 (2011).
23. J. Li, Y. Shen, and E. Y. Lam, “Hotspot-aware fast source and mask optimization,” Opt. Express **20**, 21792–21804 (2012).
24. A. Poonawala and P. Milanfar, “Mask design for optical microlithography — an inverse imaging problem,” IEEE Trans. Image Process. **16**, 774–788 (2007).
25. V. N. Mahajan, *Aberration Theory Made Simple*, 2nd ed. (SPIE, 2011, Chap. 1).
26. C. Mack, *Fundamental Principles of Optical Lithography: The Science of Microfabrication* (Wiley, 2007, Chap. 3).
27. P. Evanschitzky, F. Shao, T. Fühner, and A. Erdmann, “Compensation of mask induced aberrations by projector wavefront control,” in *Optical Microlithography XXIV*, M. V. Dusa, ed. (2011), vol. 7973 of *Proc. SPIE*, p. 797329.
28. M. K. Sears, J. Bekaert, and B. W. Smith, “Lens wavefront compensation for 3D photomask effects in subwavelength optical lithography,” Appl. Opt. **52**, 314–322 (2013).
29. N. Jia and E. Y. Lam, “Machine learning for inverse lithography: using stochastic gradient descent for robust photomask synthesis,” J. Opt. **12**, 045601 (2010).
30. Y. Shen, N. Jia, N. Wong, and E. Y. Lam, “Robust level-set-based inverse lithography,” Opt. Express **19**, 5511–5521 (2011).
31. J. Nocedal and S. J. Wright, *Numerical Optimization*, 2nd ed. (Springer, 2006, Chap. 5).
32. Y. Deng, Y. Zou, K. Yoshimoto, Y. Ma, C. E. Tabery, J. Kye, L. Capodieci, and H. J. Levinson, “Considerations in source-mask optimization for logic applications,” in *Optical Microlithography XXIII*, M. V. Dusa and W. Conley, eds. (2010), vol. 7640 of *Proc. SPIE*, p. 76401J.
33. J.-C. Yu, P. Yu, and H.-Y. Chao, “Library-based illumination synthesis for critical CMOS patterning,” IEEE Trans. Image Process. **22**, 2811–2821 (2013).
34. X. Wu, S. Liu, J. Li, and E. Y. Lam, “Efficient source mask optimization with Zernike polynomial functions for source representation,” Opt. Express **22**, 3924–3937 (2014).

#205715 - $15.00 USD Received 29 Jan 2014; revised 4 Apr 2014; accepted 4 Apr 2014; published 11 Apr 2014
(C) 2014 OSA

1. Introduction

Continuous development of advanced computational lithography techniques are required to reduce the deterioration of image fidelity and increase the process window (PW) in ultra low-k_1 optical lithography [1]. One of the limitations to PW is the noticeable difference in best focus among various feature sizes [2, 3]. This best focus shift effect, together with several other significant physical effects, is investigated in rigorous 3D mask simulations [4]. Confirmed by the experimental results, 3D mask topography is a leading cause of these effects that occur when the features on the mask are smaller than the illumination wavelength [3, 5]. In contrast to the thin mask model (Kirchhoff approximation approach), the thickness of the mask absorber produces phase errors among diffraction orders. These phase errors result in pitch-dependent best focus, thereby reducing the usable depth of focus (uDOF) [6, 7].

In order to accurately predict and describe the mask-induced phase effects, rigorous electromagnetic field (EMF) modeling is applied to light diffraction from the mask, taking the complete information of the mask topography and its material properties into account. Several well known numerical algorithms of solving Maxwell's equations, such as finite-difference time domain (FDTD) [8], rigorous coupled wave analysis (RCWA) [9] or the waveguide method [10] are used to model the light propagation through the mask in optical lithography. Unfortunately, the convergence of rigorous methods depends on mesh setting, accuracy requirements and boundary conditions [11]. As a consequence, high accuracy is achieved at a large computational cost, which limits the wide adoption of rigorous 3D mask modeling for practical large layout simulations in advanced resolution enhancement techniques (RETs) such as source and mask optimization (SMO) [12, 13].

SMO is considered as a way to obtain higher image fidelity and improved performance on process aberration stability to a given design, as 22 nm feature generation and beyond are expected to run on current immersion lithography technology [14–16]. Nevertheless, although SMO provides more flexibility regarding both the mask design and illumination configuration adjustment, it is inadequate to control the phase in the lens pupil [17–19]. To compensate for the phase errors induced by mask topography effects, additional degrees of freedom are required in terms of phase manipulation. It is now necessary to incorporate the phase parameter into source and mask optimization, a process known as mask-topography-aware source and mask optimization (mask-topography-aware SMO).

This paper focuses on a robust algorithm using inverse synthesis technique to co-optimize the source and the mask, and the major contributions are twofold. First, unlike SMO, the proposed scheme takes advantage of the fact that pupil phase manipulation can partially compensate for thick mask topography effects [20]. It incorporates some helpful pupil aberration terms such as primary and secondary spherical aberrations through statistical model of Zernike polynomials, resulting in the optimal source and mask that are not only robust against specific pupil aberration, but are also robust against similar imaging effects caused by mask topography. We demonstrate the better algorithmic performance with fewer pattern errors. Second, in terms of process robustness, we achieve a larger uDOF compared to the SMO method without considering pupil wavefront function. This is fulfilled by introducing the lens pupil plane as an additional parameter. In addition, the whole optimization procedure is performed based on the thin mask model, which ensures that the speed is faster than that based on rigorous model. To verify the practicability and effectiveness of the algorithm, we compare all the printed image fidelity and PW through rigorous EMF simulations.

2. Forward imaging model with aberration

A critical step in computational lithography is to model the imaging process accurately, with the various parameters available for adjustment. To include the pupil aberrations such that they

occur in the practical lithography process, the aerial image $I_a(x,y)$ under a partially coherent illumination (PCI) system can be described as [21]

$$I_a(x,y) = \iint_{-\infty}^{\infty} J(f,g) \left| \iint_{-\infty}^{\infty} \hat{H}(f+f_1, g+g_1) \mathrm{e}^{i2\pi W(\rho,\theta)} \hat{M}(f_1,g_1) \mathrm{e}^{-i2\pi(f_1 x + g_1 y)} \,\mathrm{d}f_1 \,\mathrm{d}g_1 \right|^2 \mathrm{d}f \,\mathrm{d}g. \tag{1}$$

In Eq.(1), $\hat{M}$ represents the spectrum of input mask pattern $M(x,y)$, and $\hat{H}$ is the ideal pupil function of the optical system under nominal conditions. The wavefront aberration function, denoted by $W(\rho,\theta)$, is incorporated by multiplying an exponential term with it as power in the frequency domain. The parameter ρ indicates the relative radial pupil position, while θ is the polar angle, represented by $\rho = \sqrt{f^2+g^2}$ and $\theta = \arctan(g/f)$. The function $J(f,g) \geq 0$ represents the effective source, which is normalized by its total energy [22,23], i.e.,

$$J(f,g) = \frac{J'(f,g)}{\iint_{-\infty}^{\infty} J'(f,g) \,\mathrm{d}f \,\mathrm{d}g}, \tag{2}$$

where $J'(f,g)$ is an arbitrary source point.

For image computation, we use the discrete form of Eq. (1), given approximated by

$$I_a(x,y) \approx \frac{\sum_{f,g} \left\{ J'(f,g) \left| M(x,y) * H(x,y) \right|^2 \right\}}{\sum_{f,g} J'(f,g)}. \tag{3}$$

We obtain the aberrated point spread function $H(x,y)$ by taking the inverse Fourier transform ($\mathscr{F}^{-1}$) of the pupil function with aberrations, i.e.,

$$H(x,y) = \mathscr{F}^{-1} \left\{ \hat{H}(f,g) \mathrm{e}^{i2\pi W(\rho,\theta)} \right\}. \tag{4}$$

The photoresist is exposed according to the intensity distribution of the aerial image $I_a(x,y)$ and developed to form the printed image $I(x,y)$. Approximating the resist effect with a sigmoid function due to its differentiability [24], the output $I(x,y)$ is given by

$$I(x,y) = \mathrm{sig}\left\{ I_a(x,y) \right\} = \frac{1}{1+\mathrm{e}^{-\alpha[I_a(x,y)-t_r]}}, \tag{5}$$

in which t_r is the threshold and α indicates the steepness of the sigmoid function.

3. Mask-topography-aware source and mask optimization algorithm

The objective of our work is to devise a method that incorporates pupil aberrations into source mask corrections to compensate for photomask topography degraded uDOF. In this section, first we describe how to design a pupil aberration function including specific aberration terms to effectively compensate 3D mask effects and analyze the rationale behind it. Then, with the aberrated transfer function, the mask and source updates are performed alternately until the termination criterion is reached.

3.1. Aberration-aware pupil function

Deviation of wavefronts, also known as aberration, represents the difference between the optical path lengths of the ray under consideration and the chief ray in traveling from the point object

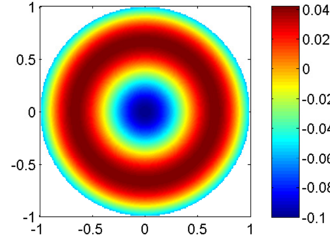

Fig. 1. Pupil wavefront distribution: a combination of primary and secondary spherical aberration.

to the reference sphere [25]. The circular wavefront profiles associated with aberrations can be mathematically modeled using Zernike polynomials [26], defined as

$$W(\rho,\theta) = \sum_{i=-\infty}^{\infty} z_i F_i(\rho,\theta), \tag{6}$$

where $F_i(\rho,\theta)$ is the ith polynominal term with z_i being the ith Zernike coefficient. In general, the Zernike functions are orthogonal in the pupil space, but not in the image space. However, sufficiently small aberrations, as they occur in lithographic projection systems, are almost linear independent in the image space as well. Thus individual aberration contributions to an overall wavefront can be isolated and quantified separately in this work.

Previous studies have found that mask topography effects have similar impact on the lithography imaging performance to those caused by wave aberrations [27, 28]. Consequently, the mask-induced phase deformation can be partially compensated by a manipulation of the pupil lens [20]. Indeed, the simulation results exhibit that primary spherical aberrations (Zernike term z_9) have the highest sensitivity, which means a large impact on linewidth through focus, and 1D lines are also prone to be affected by other spherical aberrations such as secondary spherical (Zernike term z_{16}) since the spherical aberrations have radially dependent and rotationally symmetric form [28]. Although inclusion of other Zernike terms, such as astigmatism, may provide a further improvement, the run time will also increase along with it. The wavefront function $W(\rho,\theta)$ in this work is therefore composed of spherical and secondary spherical aberrations to improve the imaging performance, as

$$W(\rho,\theta) = z_9\left(6\rho^4 - 6\rho^2 + 1\right) + z_{16}\left(20\rho^6 - 30\rho^4 + 12\rho^2 - 1\right). \tag{7}$$

A pupil wavefront distribution which combines a $z_9 = -0.08$ value of primary spherical aberration and a $z_{16} = 0.02$ value of secondary spherical aberration is shown in Fig. 1.

Substituting Eq. (7) into Eq. (4), we then use $H(x,y;z_9,z_{16})$ to represent the point spread function with primary and secondary spherical aberrations, given by

$$H(x,y;z_9,z_{16}) = \mathscr{F}^{-1}\left\{\hat{H}(f,g)\mathrm{e}^{i2\pi\left[z_9(6\rho^4-6\rho^2+1)+z_{16}(20\rho^6-30\rho^4+12\rho^2-1)\right]}\right\}. \tag{8}$$

After designing the pupil aberration function, we need to choose the Zernike coefficient values for the corresponding Zernike polynomials, which are the wavefront errors in wavelengths and are presented in units of waves. For instance, a coefficient of 0.1 means an aberration with the maximum value at $0.1\lambda = 0.1 \times 193\,\mathrm{nm} = 19.3\,\mathrm{nm}$ [28].

#205715 - $15.00 USD Received 29 Jan 2014; revised 4 Apr 2014; accepted 4 Apr 2014; published 11 Apr 2014
(C) 2014 OSA

To determine the Zernike coefficient values, we treat the aberration as a statistical model. Based on the description in Ref. [29,30], it is a reasonable assumption to model the coefficients as independent, normally distributed random variables with zero mean and identical non-zero variance. One obvious advantage of doing so is that it is not necessary to spend time seeking the optimized coefficient; after all, there may not exist a definite coefficient value beneficial for all the different feature sizes. Compared with the exhaustive search method in Ref. [28], the statistical model is more suitable for SMO, because during the iterative process of SMO, the mask pattern changes for every update and the imaging impact induced by mask topography goes with it. Hence, chances are that the optimal Zernike coefficients z_9 and z_{16} found for target pattern are different from those for the optimized mask resulting from SMO. Additionally, this caters for not only the nominal condition or certain aberration but optimizes over a range of variations. The objective function takes expectations of a weighted sum of the nominal and the aberration terms to optimize the average performance of layouts, in which the weighting coefficients are determined by the statistical probability of aberration terms appearing over a range. Therefore, this strategy compensates for both the lens aberrations and thick mask induced aberrations.

3.2. *Source mask optimization framework for statistical model*

Given the mask patterns, we not only consider the impact of the coefficient of primary spherical aberration on the compensation for 3D mask effects, but also select secondary spherical aberration to enable further tuning of the contributions of higher diffraction order. During the following process of source and mask optimization, the printed image $I(x,y;z_9,z_{16})$ is calculated under the circumstance of the spherical aberrated pupil, rather than an ideal pupil without any aberrations.

To achieve the smallest accumulated pattern error, we generate the optimal source mask pair by minimizing the sum of the mismatches between the printed image and the desired one over all locations. The expectation of the difference with respect to primary and secondary spherical aberrations is minimized to find the optimal solutions that are robust to process variations. Mathematically, the mask-topography-aware SMO minimization problem is formulated by a statistical model as

$$\begin{aligned} \underset{\mathbf{m}}{\text{minimize}} \quad & \mathscr{E}\left\{ \left\| I(x,y;z_9,z_{16}) - I_0(x,y) \right\|_2^2 \right\} \\ \text{subject to} \quad & M(x,y) \in \{0,1\}, \\ & J(f,g) \geq 0, \end{aligned} \tag{9}$$

where $\mathscr{E}\{\cdot\}$ takes the expectation operation in a range of z_9 and z_{16}. However, it is difficult to calculate the expectation integral due to the nonlinearity of the square of the ℓ_2 norm. To address this issue, we discretize z_9 to take on a set of values z_{9m} with probability $p(z_{9m})$, and the discretization for z_{16} follows a similar approach, a set of z_{16} with probabilities $p(z_{16n})$. Since the maximum optimization of wavefront deformation by the lens manipulation may be limited, restricted boundary conditions must be used during optimization, thus both z_9 and z_{16} are treated as normally distributed random variables within $[-0.1, 0.1]$ in this work with standard deviation 0.05. This leads to the following cost function

$$\mathscr{E}\left\{ \left\| I(x,y;z_9,z_{16}) - I_0(x,y) \right\|_2^2 \right\} \approx \sum_{m,n} p(z_{9m}) p(z_{16n}) \left\{ \left\| I(x,y;z_{9m},z_{16n}) - I_0(x,y) \right\|_2^2 \right\} \tag{10}$$

Gradient methods are frequently used to tackle the optimization problem iteratively. Here we define the differential operator $\nabla F(a)$ to evaluate the gradient of a function F with respect to its argument a in the discrete domain, due to the discrete nature of the mask and

#205715 - $15.00 USD Received 29 Jan 2014; revised 4 Apr 2014; accepted 4 Apr 2014; published 11 Apr 2014
(C) 2014 OSA

source. In mask-topography-aware SMO, we first compute two gradients: one is the derivative of $\left\|I(x,y;z_{9m},z_{16n})-I_0(x,y)\right\|_2^2$ with respect to an arbitrary source point $J'(f,g)$, and the other one is the derivative with respect to the mask $M(x,y)$, respectively denoted as $\nabla\mathscr{F}_{m,n}(J')$ and $\nabla\mathscr{F}_{m,n}(M)$. As shown in the Appendix, these are given by

$$\nabla\mathscr{F}_{m,n}(M)=\sum_{f,g}J(f,g)\odot\mathrm{Re}\left\{\left[2\alpha(I-I_0)\odot I\odot(1-I)\odot\left(M*H(x,y;z_{9m},z_{16n})\right)^{\dagger}\right]*\tilde{H}\right\},\tag{11}$$

$$\nabla\mathscr{F}_{m,n}(J')=\sum_{x,y}2\alpha(I-I_0)\odot I\odot(1-I)\odot\frac{\left|M*H(x,y;z_{9m},z_{16n})\right|^2-I_a}{\sum_{f,g}J'(f,g)},\tag{12}$$

where $\tilde{H}(x,y;z_{9m},z_{16n})=H(-x,-y;z_{9m},z_{16n})$, and symbol $\dagger$ is a complex conjugate operator and $\odot$ indicates pixel-by-pixel multiplication.

We then sum it for all values of m and n to incorporate the possible primary and secondary spherical variations. Hence, the gradients of $\mathscr{E}$ we need are

$$\nabla\mathscr{E}_{m,n}(M)=\sum_{m,n}p(z_{9m})p(z_{16n})\nabla\mathscr{F}_{m,n}(M),\tag{13}$$

$$\nabla\mathscr{E}_{m,n}(J')=\sum_{m,n}p(z_{9m})p(z_{16n})\nabla\mathscr{F}_{m,n}(J').\tag{14}$$

The optimization is solved iteratively using nonlinear conjugate-gradient (CG) methods [31], and the updating process is similar to our previous work in Refs. [22] and [23]. The target pattern is assigned as the initial mask, and the first mask optimization is performed with a fixed traditional annular illumination. SMO works by alternating between optimizing the mask given the source, and updating the source by keeping the mask fixed, and repeating these two steps until a stopping criterion is satisfied.

We now explain in detail how the mask and source optimization are performed. First, we calculate the gradient with respect to M, as in Eq. (13), and then update the scalar $\alpha_m^{(k)}$, given by

$$\alpha_m^{(k)}=\frac{\nabla\mathscr{E}_{m,n}(M)^{(k)}\left(\nabla\mathscr{E}_{m,n}(M)^{(k)}-\nabla\mathscr{E}_{m,n}(M)^{(k-1)}\right)}{\left(\nabla\mathscr{E}_{m,n}(M)^{(k)}-\nabla\mathscr{E}_{m,n}(M)^{(k-1)}\right)r_m^{(k-1)}},\tag{15}$$

where the superscript k with brackets denotes the kth iteration, and $r_m^{(0)}=0$ in the initialization step. Next, we compute the residual $r_m^{(k)}$ at the kth step by

$$r_m^{(k)}=-\nabla\mathscr{E}_{m,n}(M)^{(k)}+\alpha_m^{(k)}r_m^{(k-1)},\tag{16}$$

which ensures the directions are always descending for the cost function. Finally, the current mask is obtained by

$$M^{(k+1)}=M^{(k)}+s_1r_m^{(k)},\tag{17}$$

where s_1 is a small constant known as the step size.

The above steps are mask optimization procedure, which will run for a pre-defined number of iterations, and the resulting optimal mask is then used during the following source updates. The core of the source optimization follows a similar approach, except for using the gradient expressions in Eq. (12) and Eq. (14), and the step size s_2 is set for updating the source, given

#205715 - $15.00 USD Received 29 Jan 2014; revised 4 Apr 2014; accepted 4 Apr 2014; published 11 Apr 2014
(C) 2014 OSA

by

$$\alpha_s^{(k)} = \frac{\nabla \mathscr{E}_{m,n}(J')^{(k)} \left(\nabla \mathscr{E}_{m,n}(J')^{(k)} - \nabla \mathscr{E}_{m,n}(J')^{(k-1)} \right)}{\left(\nabla \mathscr{E}_{m,n}(J')^{(k)} - \nabla \mathscr{E}_{m,n}(J')^{(k-1)} \right) r_s^{(k-1)}}, \tag{18}$$

$$r_s^{(k)} = -\nabla \mathscr{E}_{m,n}(J')^{(k)} + \alpha_s^{(k)} r_s^{(k-1)}, \tag{19}$$

$$J^{(k+1)} = J^{(k)} + s_2 r_s^{(k)}. \tag{20}$$

The updating steps of source optimization is described in the above three equations, which will also run for a fixed number of iterations and output the optimal source to the succeeding mask updates. Then the mask optimization and source optimization are performed alternately until we check if the overall stop condition is satisfied; if not, the mask optimization procedure and source optimization procedure are performed again. Otherwise, a final mask optimization is run to generate a new source-mask pair.

4. Results

To evaluate the performance of the proposed mask-topography-aware SMO algorithm, we compare and analyze the simulation results in terms of pattern error and usable depth of focus. Two kinds of target patterns are used: a vertical line/space design with three different pitches and alternatively arranged brick poly array, as shown in Fig. 2. All images are represented by a 151×151 matrix with a pixel size of $4\,\text{nm} \times 4\,\text{nm}$ and critical dimension (CD) of $32\,\text{nm}$; the absorbers are composed of two layers, $55\,\text{nm}$ of Cr ($n = 1.477/k = 1.762$) below $18\,\text{nm}$ of CrO ($n = 1.965/k = 1.201$). An annular illumination composed of 21×21 pixels with its inner annulus $\sigma_{in} = 0.7$ and outer annulus $\sigma_{out} = 0.9$ is adopted as the initial value for our source optimization. The parameters of the projection system are set to be $\lambda = 193\,\text{nm}$ and $\text{NA} = 1.35$. In the sigmoid function, t_r is equal to 0.3 for Kirchhoff approximation simulation, while given the intensity losses induced by mask topography, it is determined according to the intensity distribution of the aerial image $I_a(x,y)$ in rigorous mask model computation. In addition, for a certain circuit pattern, we assign the same t_r value for both conventional SMO and mask-topography-aware SMO in rigorous simulations.

In order to evaluate the image fidelity, we compare the optimization results using our proposed mask-topography-aware SMO framework with an SMO with ideal pupil, where the line/space pattern in Figs. 2(a) – 2(c) are used as input. All simulations and process window analysis in this Section are performed using the Fraunhofer IISB development and research lithography simulator Dr.LiTHO, which computes the mask near fields through the waveguide method [4]. Here, we firstly analyze the optimization results for the vertical lines at 112 nm pitch, while the other two results will be given in the following description. Figures 3(a) – 3(c) respectively display the resulting source, the optimized mask and the printed image at nominal conditions using the conventional SMO. The corresponding results from the robust SMO with spherical aberrations are given in the following row with the same structure. Comparing the circuit images shown in Figs. 3(c) and 3(f), we observe that not only the end regions but also the middle lines in the former have more distortions, which signifies that our method has a better resolution enhancement capacity over such regions. It can also be seen from the comparison of Figs. 3(a) and 3(d) that inclusion of Zernike term of spherical aberration in the optimization procedure can provide a more reasonable source shape, since source points along the horizontal axis are helpful in printing vertical lines and spaces [32–34]. All the optimized sources are normalized by the maximum pixel intensity for better visualization.

Simulation is also conducted with the other kind of pattern: brick poly array in Fig. 2(d) as input, using our proposed SMO framework and conventional SMO without applied wavefront

#205715 - $15.00 USD Received 29 Jan 2014; revised 4 Apr 2014; accepted 4 Apr 2014; published 11 Apr 2014
(C) 2014 OSA

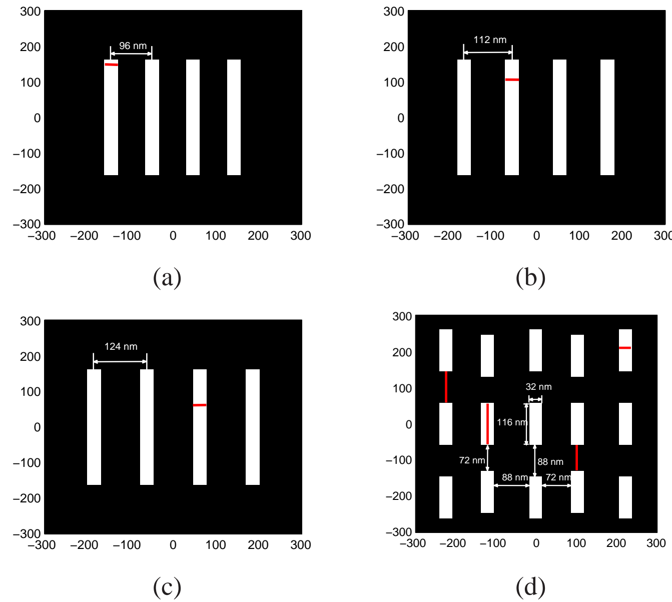

Fig. 2. Two kinds of test patterns used in simulation: (a)–(c) vertical line/space design with different pitches and (d) brick poly array. Red lines mark the critical locations for measuring the process window.

aberrations. This can be regarded as further evidence that the circuit pattern quality is indeed improved by mask-topography-aware SMO. Figure 4 presents the corresponding results in a way similar to the above. It is worth noting that printed image fidelity in Fig. 4(f), using the proposed SMO including Zernike terms z_9 and z_{16}, is improved, showing 66% reduced pattern errors than that in Fig. 4(c). Especially for the four polys located in the four corners of the image, SMO nearly fails to print them, which is likely to disable the circuit from functioning normally. In contrast, they can achieve a much better shape during mask-topography-aware SMO.

Table 1 summarizes the measurement of the pattern errors for the two kinds of test patterns, where we compute the mask near fields with Kirchhoff thin mask model and thick mask model respectively. For each model, we compare the results from the two methods. Because the whole optimization procedure is performed based on the thin mask model, the optimal source mask pairs resulting from SMO and mask-topography-aware SMO produce similar pattern errors in Kirchhoff approximation simulation. Although they both have “good enough” performance for thin mask, they lead to distinguishing outputs for rigorous simulations, where reduced pattern errors indicate an improved image fidelity. For all the test patterns, mask-topography-aware SMO can achieve a better performance in rigorous simulations, reducing the pattern errors by 14% to 66%. In particular, dense features represented by 96 nm pitch have the biggest difference between the two methods. This is consistent with our observation in the aerial images of Figs. 5(b) and 5(d). This result is related to the fact that SMO does not generate helpful assisted features in the optimal mask, which has no significant impact on image in thin mask model computation. However, for rigorous simulation, the absence of assisted features causes undesired sidelobe printing and there is no safe intensity at which the sidelobes do not print, as illustrated in Fig. 5(b). Accordingly, incorporating sensitive aberrations terms in mask-topography-aware SMO allows a more robust design against the mask-induced aberrations.

#205715 - $15.00 USD Received 29 Jan 2014; revised 4 Apr 2014; accepted 4 Apr 2014; published 11 Apr 2014
(C) 2014 OSA

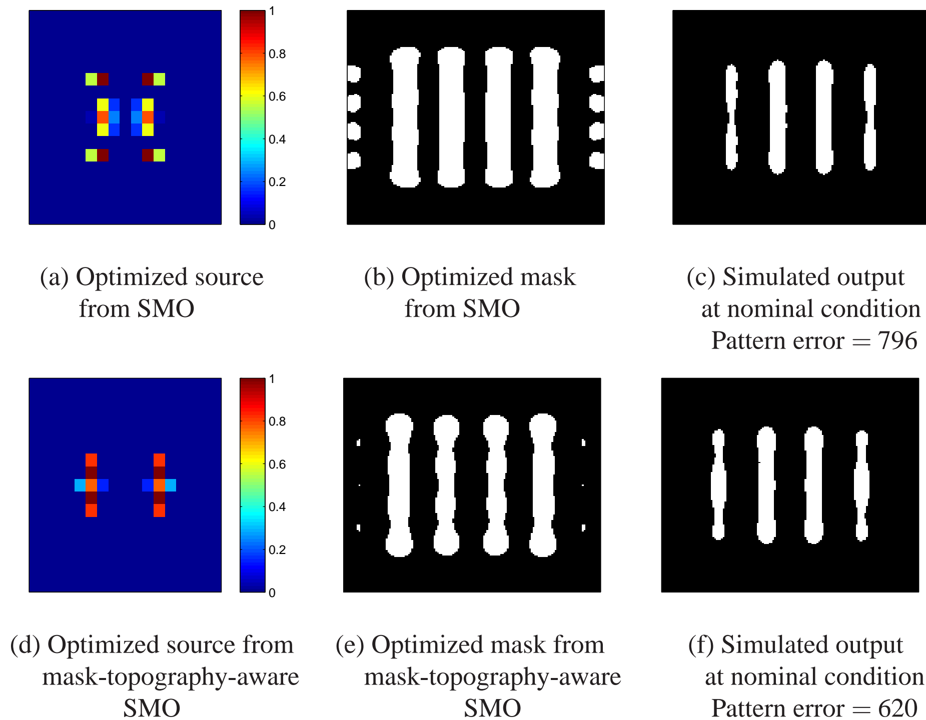

(a) Optimized source from SMO

(b) Optimized mask from SMO

(c) Simulated output at nominal condition Pattern error = 796

(d) Optimized source from mask-topography-aware SMO

(e) Optimized mask from mask-topography-aware SMO

(f) Simulated output at nominal condition Pattern error = 620

Fig. 3. Simulation results of 32 nm vertical lines at 112 nm pitch.

Moreover, we compare with another approach where the pupil is manipulated after the SMO, which is called source-mask-pupil optimization (SMPO) [18]. We run the simulations using the optimal sources and masks resulting from SMO to see the pattern error change versus z_9 coefficients, as plotted in Fig. 6. For both cases, it can be observed from Fig. 6 that when z_9 changes within $[-0.1, 0.1]$, all the pattern errors resulting from the SMO approach are larger than those from mask-topography-aware SMO. In other words, even if the pupil wavefront receives further control after SMO, the proposed robust SMO algorithm, which incorporates pupil spherical aberrations into the source and mask optimization processes, can still deliver a better design. This verifies that a combination of z_9 and z_{16} in the way shown in our method would provide compensation effectively. Furthermore, Fig. 6 also shows that the statistical aberration model adopted in our method is not only applicable to a certain aberration condition, but optimizes the performance over a range of spherical variations. As a result, even if the optimal z_9 coefficient is not known in advance, the proposed SMO algorithm with statistical model can still deliver a better design which is robust to spherical aberration. The above simulation results also affirm that the proposed mask-topography-aware SMO is capable of compensating for both thick mask induced aberration and lens aberrations.

After evaluating the image quality of different algorithms, we can now assess the robustness of the proposed algorithm in terms of the process window. Figure 7 depicts the average exposure-defocus window comparison for line/space pattern involving SMO without pupil aberration versus mask-topography-aware SMO. For each pitch, the middle line represents the dose values to create the target linewidth, and the other two respectively correspond to the maximum and minimum doses with linewidth change within 10% [4]. The minimum feature size (also the width of the feature) is chosen as the critical regions, as marked by the red lines in

#205715 - $15.00 USD Received 29 Jan 2014; revised 4 Apr 2014; accepted 4 Apr 2014; published 11 Apr 2014
(C) 2014 OSA

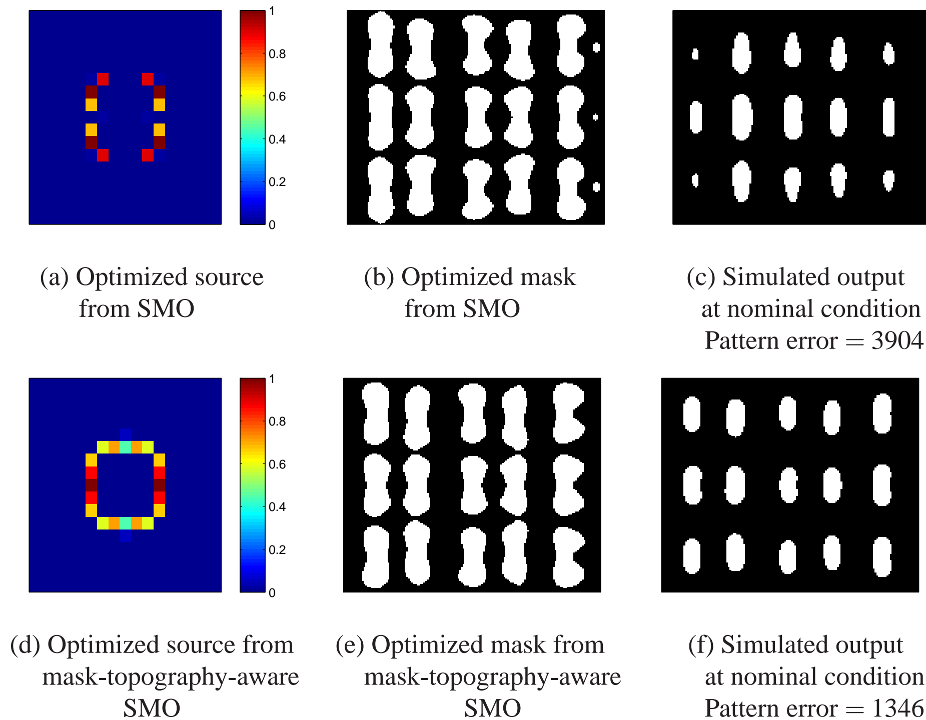

(a) Optimized source from SMO

(b) Optimized mask from SMO

(c) Simulated output at nominal condition Pattern error = 3904

(d) Optimized source from mask-topography-aware SMO

(e) Optimized mask from mask-topography-aware SMO

(f) Simulated output at nominal condition Pattern error = 1346

Fig. 4. Simulation results of brick poly array pattern.

Figs. 2(a) – 2(c). With no pupil wavefront aberration, the vertical lines at three different pitches have no overlapping process windows caused by deviation in the best exposure dose, as shown in Fig. 7(a). In comparison, a larger uDOF is observed in Fig. 7(b), where the proposed SMO algorithm including both z_9 and z_{16} coefficients increases the process capability by producing a 60 nm larger defocus range than the conventional SMO method, demonstrating enhanced process robustness.

Another noticeable change is that both 96 nm and 112 nm pitch lines resulting from SMO have obvious best focus shift, as illustrated by blue solid lines and green dotted lines in Fig. 7(a). Rigorous computation exhibits an asymmetry in the curve, whereas the process windows obtained with mask-topography-aware SMO corrects the focus shift for both configurations. Such results are reasonable because the consideration of pupil wavefront, in the form of spherical aberration in the optimization procedure, can adjust the phase shift induced by the thick absorber, thereby compensating for pitch dependent best focus and increasing uDOF. Figure 8 exhibits similar improvements of PW for brick poly array. For three critical locations, namely, 88 nm gap (position 1), 116 nm height (position 2) and 72 nm gap (position 3), the degraded uDOF is increased from 0 nm for SMO in Fig. 8(a) to 60 nm with wavefront aberration correction in Fig. 8(b). Furthermore, process window of 88 nm and 72 nm gap have negative best focus shift, while position 2 shifts in the opposite direction in Fig. 8(a). This best focus variation is decreased through the proposed robust SMO method. Note that Fig. 8(a) can hardly obtain the magenta curves that represent the process window of 32 nm poly width (position 4), which means that once the focus changes, SMO cannot output a feasible design, while our method keeps the feature size changing within 10%. Similar situations can also be seen in Fig. 7(a), where the blue curves vanish when the defocus exceeds 64 nm. These results are essentially in

Table 1. Comparison of performance with different models and methods.

Test patterns	Pitch (nm)	Model	Methods	PE (pixels)
Vertical lines	96	Kirchhoff model	SMO	88
			mask-topography-aware SMO	100
		Rigorous model	SMO	2630
			mask-topography-aware SMO	948
	112	Kirchhoff model	SMO	56
			mask-topography-aware SMO	204
		Rigorous model	SMO	796
			mask-topography-aware SMO	620
	124	Kirchhoff model	SMO	102
			mask-topography-aware SMO	84
		Rigorous model	SMO	820
			mask-topography-aware SMO	708
Brick poly array		Kirchhoff model	SMO	391
			mask-topography-aware SMO	415
		Rigorous model	SMO	3904
			mask-topography-aware SMO	1346

agreement with the conclusions in Ref [28], i.e., the through-pitch best focus difference induced by thick mask topography can be corrected effectively by applying pupil aberration functions in the lens domain.

5. Conclusion

In this paper, a robust mask-topography-aware SMO algorithm is presented for thick mask compensation in optical lithography. We apply the approach to 1D vertical line/space patterns with different pitches, as well as to 2D features. Evaluations against SMO without incorporating pupil aberrations demonstrate that the combination of primary and secondary spherical aberration terms deliver advantages such as high image fidelity, reduced best focus difference and improved uDOF. This allows pupil aberration-aware source and mask co-optimization, to be a prime candidate for computational lithography especially with the increasing severity of mask-induced effects and the demand for highly accurate and fast simulations in the future.

A. Appendix: Gradients derivation

Here we compute the derivatives of the cost function in Eqs. (11) and (12). Due to the discrete nature of the source and mask, the differential operator$\partial/\partial M$ and $\partial/\partial J'$ are approximated by numerical differences.

The first gradient of the pattern fidelity term $\left\|I(x,y;z_{9m},z_{16n})-I_0(x,y)\right\|_2^2$ with respect to the

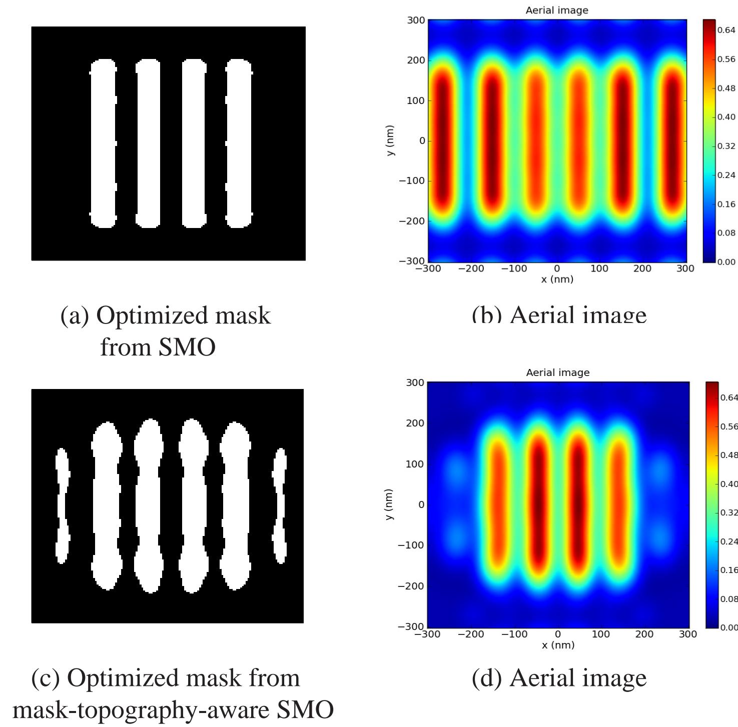

(a) Optimized mask from SMO (b) Aerial image

(c) Optimized mask from mask-topography-aware SMO (d) Aerial image

Fig. 5. Simulated aerial image of 32 nm vertical lines at 96 nm pitch.

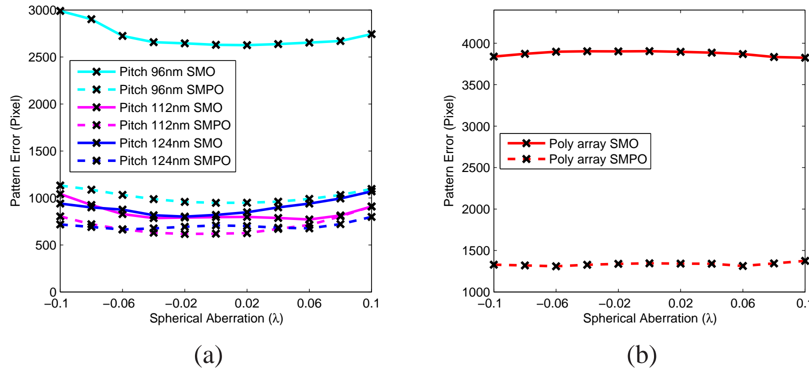

(a) (b)

Fig. 6. Simulated pattern errors at different primary spherical aberration values (z_9) for: (a) vertical line/space with different pitches and (b) brick poly array.

mask pattern is given by

$$\begin{aligned}
\nabla \mathscr{F}_{m,n}(M) &= \frac{\partial \sum_{x,y} \|I - I_0\|_2^2}{\partial M} \\
&= \left[2\alpha(I - I_0) \odot I \odot (1 - I) \odot \frac{\partial I_a}{\partial M}\right] \\
&= \sum_{f,g} J(f,g) \\
&\quad \odot \mathrm{Re}\left\{ \left[2\alpha(I - I_0) \odot I \odot (1 - I) \odot \left(M * H(x,y;z_{9m},z_{16n})\right)^{\dagger}\right] * \tilde{H} \right\}. \qquad (21)
\end{aligned}$$

#205715 - $15.00 USD Received 29 Jan 2014; revised 4 Apr 2014; accepted 4 Apr 2014; published 11 Apr 2014
(C) 2014 OSA

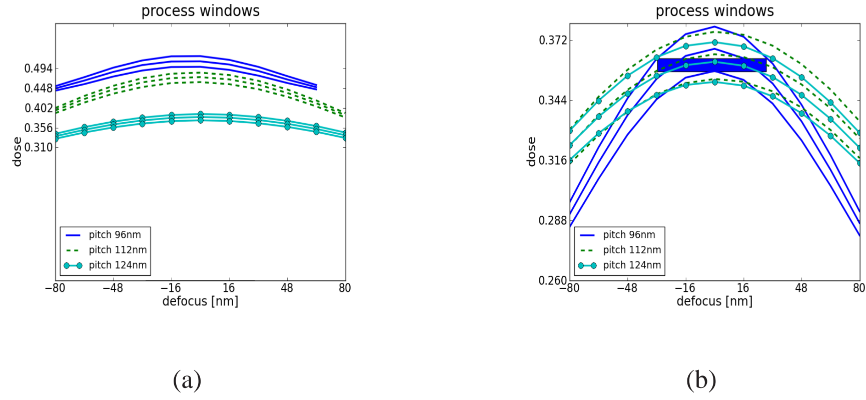

Fig. 7. Simulated process window of vertical line/space with different pitches with (a) conventional SMO without pupil aberration and (b) mask-topography-aware SMO.

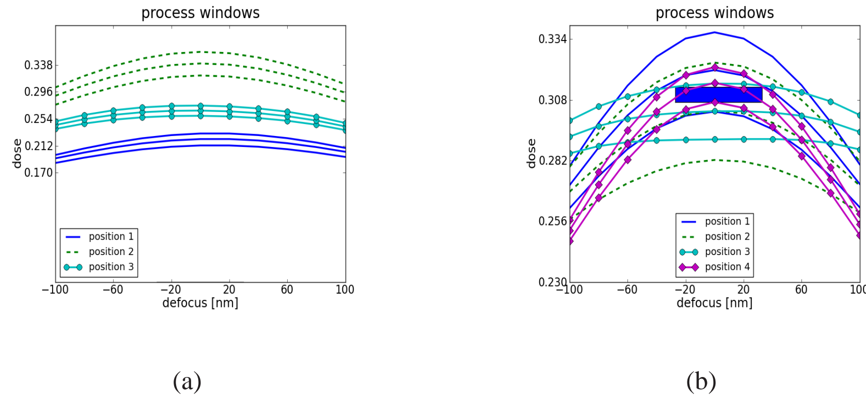

Fig. 8. Simulated process window of brick poly array with (a) conventional SMO without pupil aberration and (b) mask-topography-aware SMO.

The analytical form of the partial gradients for the illumination source in Eq. (12) is

$$\begin{aligned}
\nabla \mathscr{F}_{m,n}(J') &= \frac{\partial \sum_{x,y} \|I - I_0\|_2^2}{\partial J'} \\
&= \sum_{x,y} 2\alpha (I - I_0) \odot I \odot (1 - I) \odot \frac{\partial I_a}{\partial J'} \\
&= \sum_{x,y} 2\alpha (I - I_0) \odot I \odot (1 - I) \\
&\quad \odot \frac{\left|M * H(x,y;z_{9m},z_{16n})\right|^2 \sum_{f,g} J'(f,g) - \sum_{f,g} J'(f,g) \left|M * H(x,y;z_{9m},z_{16n})\right|^2}{\left[\sum_{f,g} J'(f,g)\right]^2} \\
&= \sum_{x,y} 2\alpha (I - I_0) \odot I \odot (1 - I) \odot \frac{\left|M * H(x,y;z_{9m},z_{16n})\right|^2 - I_a}{\sum_{f,g} J'(f,g)}. \qquad (22)
\end{aligned}$$

#205715 - $15.00 USD Received 29 Jan 2014; revised 4 Apr 2014; accepted 4 Apr 2014; published 11 Apr 2014
(C) 2014 OSA

Acknowledgments

This work was supported in part by the UGC Areas of Excellence project Theory, Modeling, and Simulation of Emerging Electronics, and by the State Key Lab of Digital Manufacturing Equipment and Technology under Project DMETKF2013003. The authors would also like to acknowledge Fraunhofer Institute for Integrated Systems and Device Technology for the use of Dr.LiTHO.